

Non-linear rheology of lamellar liquid crystals

C.-Y.D. Lu^{1,a}, P. Chen², Y. Ishii³, S. Komura^{3,b}, and T. Kato³

¹ Department of Chemistry, National Taiwan University, Taipei 106, Taiwan

² Department of Physics and Center for Complex Systems, National Central University, Jung-li 320, Taiwan

³ Department of Chemistry, Graduate School of Science and Engineering, Tokyo Metropolitan University, Tokyo 192-0397, Japan

Received 1 August 2007

Published online: 29 February 2008 – © EDP Sciences / Società Italiana di Fisica / Springer-Verlag 2008

Abstract. We measure the non-linear relation between the shear stress and shear rate in the lyotropic lamellar phase of C₁₂E₅/water system. The measured shear thinning exponent changes with the surfactant concentration. A simple rheology theory of a lamellar or smectic phase is proposed with a prediction $\dot{\gamma} \sim \sigma^{3/2}$, where $\dot{\gamma}$ is the shear rate and σ is the shear stress. We consider that the shear flow passed through the defect structure causes the main dissipation. As the defect line density varies with the shear rate, the shear thinning arises. The defect density is estimated by the dynamic balance between the production and annihilation processes. The defect production is caused by the shear-induced layer undulation instability. The annihilation occurs through the shear-induced defect collision process. Further flow visualization experiment shows that the defect texture correlates strongly with the shear thinning exponent.

PACS. 61.30.Jf Defects in liquid crystals – 83.60.Fg Shear rate dependent viscosity – 61.72.Lk Linear defects: dislocations, disclinations

1 Introduction

The rheology of lamellar or smectic liquid crystals is a long-standing puzzle [1]. A very thin free-standing layer which is very well oriented shows a medium value in the plane shear viscosity (the η_3 in the Harvard notation [2]) of the order 0.03–0.07 Pa s for rod-like molecules such as 8CB [3]. Real flows in general situations, however, are totally different, where the samples become far more viscous than the well-aligned ones. This is believed mainly due to the texture. The presence of domains, together with grain boundaries and line defects between them, is responsible for the high viscosity. Taking the finite grains as the basic unit, Kawasaki and Onuki suggested that the layer relaxation within the lamellar domains may have an important contribution to the linear viscoelasticity [4]. The detailed grain boundary or defect structures do not enter into their arguments, which indicates a high universality. Other theoretical suggestions examine the layer fluctuations within the extremely large domain [5, 6]. This fluctuation effect is estimated with a logarithmic dependence on the domain size, and should be small for the typical sample which consists of small grains. The direct visualization by Basappa *et al.* shows that the defect line density correlates strongly with the viscosity [7]. Therefore the defects must play a central role in the lamellar rheology.

Recently Meyer *et al.* have proposed a theory for lamellar viscosity which is explicitly based on the defect line motion [8–10]. They considered the screw defect line motion which produces the plastic deformation of the lamellar structure. The defect lines move between the sites of local free-energy minima, which is responsible for the dissipation. Their argument arrives at a power law behavior with the constitutive relation $\dot{\gamma} \sim \sigma^m$, with the universal shear exponent $m = 5/3$ relating the shear rate $\dot{\gamma}$ and the shear stress σ . (Here we use the notation in Refs. [9, 10] which follows the metallurgical usage. The conventional shear thinning exponent n defined by $\sigma \sim \dot{\gamma}^n$ is simply related by $n = 1/m$.) Three experimental systems, including a copolymer solution, a thermotropic smectic liquid crystal (8CB), and a lyotropic system, all support this exponent [10]. Other earlier and recent experiments on smectics or lamellar phases reported that the exponent m varies between 1 and 2 [11–16] (see Tab. 2 later). At the moment, it is not clear whether the exponent is truly universal and all these variations are due to experimental errors, or it depends on the systems studied.

In this work, we first study experimentally the lyotropic system of a non-ionic surfactant C₁₂E₅ and water. In Section 2, we discuss its non-linear rheological behavior as the temperature and concentration are varied. We find that the C₁₂E₅/water binary mixture has a shear exponent different from the systems studied by Meyer *et al.* [9, 10]. In Section 3 we propose a scaling argument

^a e-mail: cydlu@ntu.edu.tw

^b e-mail: komura@tmu.ac.jp

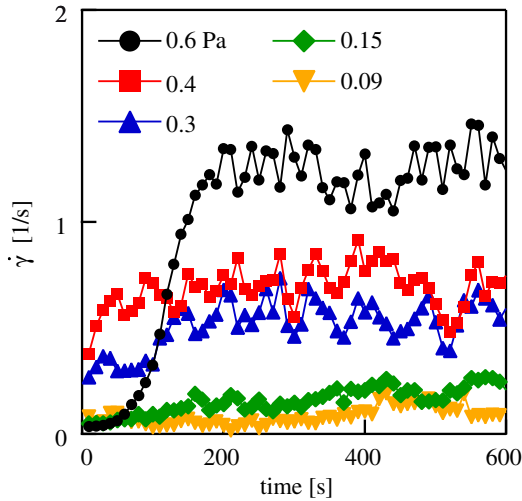


Fig. 1. (Color online) Time evolution of the measured shear rate $\dot{\gamma}$ under constant stresses $\sigma = 0.09, 0.15, 0.3, 0.4, 0.6$ Pa during 600 s for a $C_{12}E_5$ /water binary system. The surfactant composition is $\phi = 35$ wt% and the temperature is $T = 66^\circ\text{C}$ at which the system is in the lamellar phase.

for the shear exponent which operates when the defect is produced by the flow instability. We estimate the defect density by the dynamic balance between the production and annihilation processes. Our theoretical prediction for the exponent ($m = 3/2$) is in agreement with our experimental results. We reported in Section 4 a preliminary flow visualization experiment which shows the correlation between the shear exponent and the defect texture. Some discussions and the comparison with the theory by Meyer *et al.* are provided in Section 5.

2 Rheology experiment

In this section, we first present the results of rheology experiment on a lyotropic liquid crystal. The studied system is composed of a binary mixture of water and non-ionic surfactant $C_{12}E_5$ (C_nE_m represents the chemical formula $C_nH_{2n+1}(OCH_2CH_2)_m-OH$). We purchased $C_{12}E_5$ from Nikko Chemicals, Inc., and used without any further purification. The composition-temperature phase diagram of this system has been reported [17]. The rheological measurement was performed in the surfactant composition range $\phi = 30$ –45 wt% and the temperature range $T = 66$ –71 $^\circ\text{C}$. For this condition, the system is in the single lamellar phase. We used a rotational rheometer AR550 from TA Instruments, Ltd. All the measurements were carried out under constant stress σ in the cone-and-plate geometry. Here the cone is made in stainless steel. The diameter of the cone is 40 mm and the cone angle is 1.5° , while the truncation is $47\ \mu\text{m}$. No anchoring treatment was performed.

Typical time evolutions of the measured shear rate are presented in Figure 1 for different applied shear stresses when $\phi = 35$ wt% and $T = 66^\circ\text{C}$. Each stress was applied for 600 s within which the sample reached the steady state.

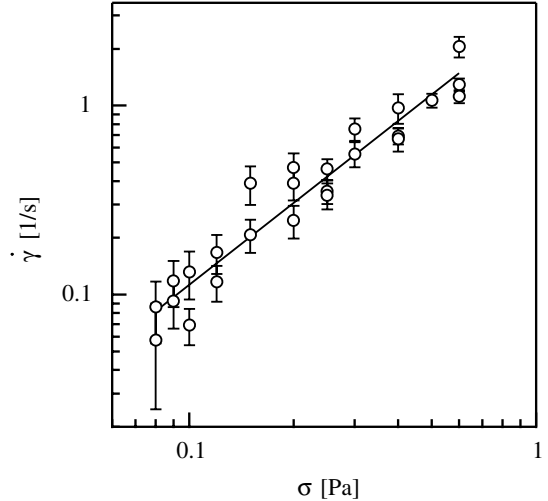


Fig. 2. Log-log plot of the steady-state shear rate $\dot{\gamma}$ (averaged over 450–600 s in Fig. 1) as a function of the shear stress σ when $\phi = 35$ wt% and $T = 66^\circ\text{C}$. The slope of the straight line is $m = 1.44 \pm 0.08$ which gives the exponent of the stress scaling behavior $\dot{\gamma} \sim \sigma^m$.

We have checked that the system attains the stationary state within 600 s by performing much longer measurements. For very small stress values such as $\sigma = 0.09$ Pa, however, the small shear rate signal interferes with an artificial oscillatory noise generated by the rheometer, and it becomes more difficult to determine the stationary state accurately. Nevertheless, we have compared the shear rate data up to 600 s for all the stress values by assuming that the system has reached the steady state. The applied shear stress was successively decreased from the higher to lower values. The sample was kept at rest for 120 s between successive measurements with different stresses. The solvent evaporation is insignificant within one sequence of the experimental time. Such a measurement has been repeated several times and the obtained data were accumulated in order to better estimate the scaling relation between the shear stress and shear rate. We have also tried to measure the shear rate by successively increasing (rather than decreasing) the shear stress from the lower to higher values. However, this was impossible without a preshearing treatment at the beginning. After preshearing the sample for several minutes, we have recovered almost the same result as presented above. Figure 2 is the log-log plot of the steady-state shear rate (averaged between 450 and 600 s) as a function of the applied stress for several sequences of the measurement. As indicated by the solid fitted line, the shear rate obeys a power law behavior $\dot{\gamma} \sim \sigma^m$, with $m = 1.44 \pm 0.08$.

Next we investigated the effect of temperature when $\phi = 35$ wt%. The measured shear rate is plotted for various temperatures in Figure 3. For each temperature, we extract the exponent m which is summarized in Table 1. For the studied temperature range, m is almost independent of the temperature within the experimental error. Then the temperature effect can be incorporated in the prefactor $A(T)$ such that $\dot{\gamma} \sim A(T)\sigma^m$, as suggested in

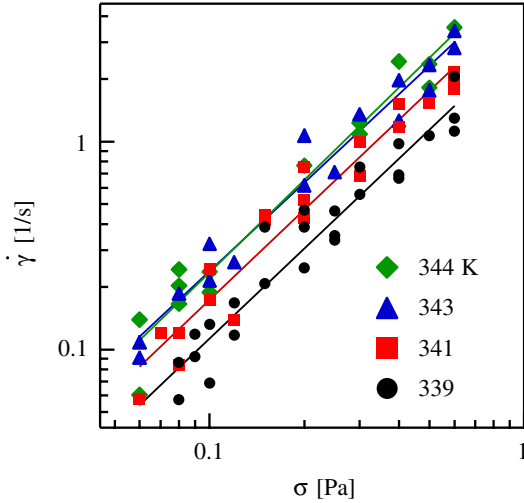


Fig. 3. (Color online) Log-log plot of the steady-state shear rate $\dot{\gamma}$ as a function of the shear stress σ at different temperatures but with fixed composition $\phi = 35$ wt%. Each slope of the straight line is almost identical to that of $T = 66$ °C (339 K) within the experimental errors.

Table 1. The values of the stress scaling exponent m defined by $\dot{\gamma} \sim \sigma^m$ for different temperatures when $\phi = 35$ wt%.

T (°C)	m
66	1.44 ± 0.08
68	1.44 ± 0.07
70	1.42 ± 0.07
71	1.48 ± 0.09

reference [9]. Here we assume that the macroscopic rheological behavior corresponds to thermally activated processes. The different values of $A(T)$ obtained from Figure 3 are plotted as a function of $1/T$ in Figure 4. From the slope of the solid line, we have determined the activation energy W defined by

$$A(T) = A_0 \exp(-W/k_B T), \quad (1)$$

where k_B is the Boltzmann constant. The obtained value is $W \approx 65k_B T_R$, with $T_R = 339$ K. This value of the activation energy is comparable to those reported in reference [9] both for thermotropic and lyotropic lamellar phases. (It should be noted that, in Ref. [9], a dilute lyotropic system of CpCl/hexanol/brine exhibits a completely different exponent; $m \approx 5$. In this case, the activation energy is much smaller.) The physical interpretation of the obtained activation energy will be discussed in Section 5.

For fixed $T = 66$ °C, we varied the composition ϕ and repeated the same measurements. The result is plotted in Figure 5 for four different compositions. Although a power law behavior is observed for each composition, the exponent m actually varies between different compositions. In Figure 6, we plotted the obtained exponents as a function of the composition, together with the theoretical predictions by Meyer *et al.* ($m = 5/3$) [9,10] and by us ($m = 3/2$, as described in the next Section). In general, the observed

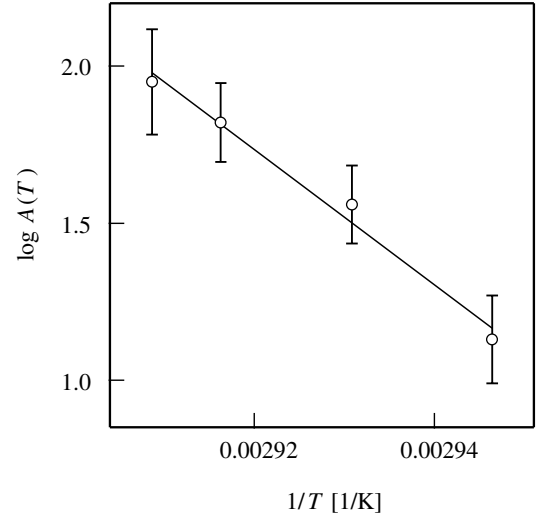


Fig. 4. Normal plot of $\log A(T)$ as a function of $1/T$ when $\phi = 35$ wt%. The slope of the straight line gives the activation energy $W \approx 65k_B T_R$, with $T_R = 339$ K (see Eq. (1) and the text).

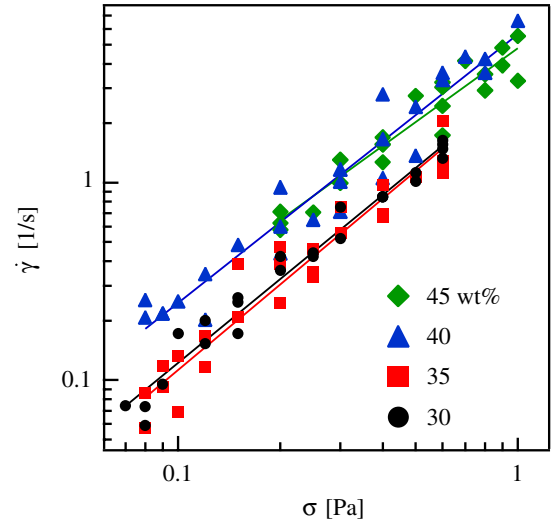


Fig. 5. (Color online) Log-log plot of the steady-state shear rate $\dot{\gamma}$ as a function of the shear stress σ at different compositions but with fixed temperature $T = 66$ °C. The slope of the straight lines differs slightly among different compositions.

exponent is close, but slightly smaller than our prediction $m = 3/2$. The deviation from $m = 3/2$ is largest when $\phi = 45$ wt% compared to the other three compositions. This result would be consistent with the observed difference in the defective textures as we shall present in Section 4. The difference may be due to a gradual structural transition in the sample, leading to a weaker shear thinning behavior. Although it is known that a dynamical transition to the so-called onion structure occurs in the presence of a relatively large shear flow [14,15], we consider that it is not the case for $\phi = 45$ wt%. This is because the exponent m would be much larger in the onion

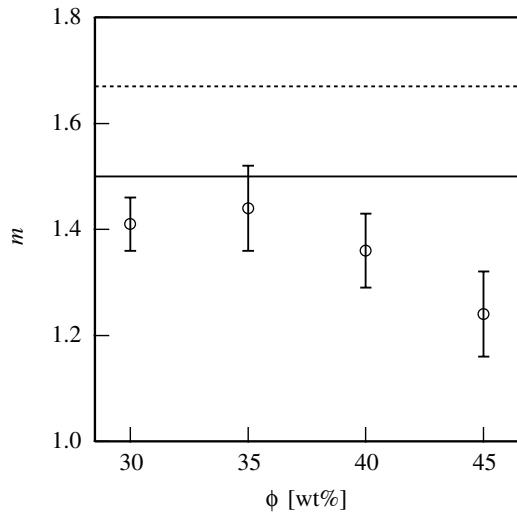


Fig. 6. The exponent m as a function of the composition. The solid line is our theoretical prediction $m = 3/2$ while the dashed line corresponds to $m = 5/3$ which is predicted by Meyer *et al.* in references [9,10].

phase, and the texture of the $\phi = 45$ wt% sample (see later Fig. 12(d)) does not indicate any onion formation.

Table 2 summarizes the reported values of m in the literature for various smectic or lamellar phases including both thermotropic and lyotropic cases. The temperature range is specified for a thermotropic liquid crystal 8CB reported in different papers. When the system undergoes a structural transition, we picked up the exponent that characterizes the weak shear regime. Here m typically ranges between 1 and 2 but its precise value is not yet determined.

3 Theory

3.1 Dislocation loop under shear flow

In this section we present our scaling argument on defect dynamics, which predicts the exponent $m = 3/2$ as mentioned above. The screw defects in lamellar or smectic phases cost very small free energy compared with the edge defects. Therefore the tangent direction of the screw defects will remain perpendicular to the layers even in the presence of a gentle shear. The two extremities of a screw defect line will experience different ambient velocity under the shear flow. If the two edges linked to the two ends of the screw have their tangents perpendicular to the flow velocity (pointing along the vorticity direction), the flow will have different relative velocity to the two edges. This relative flow introduces the dissipation similar to the situation of edge climbing. Following Oswald and Allain [18], we regard this as the major dissipation. The viscous stress therefore depends on the defect density.

To evaluate the defect density at a given shear rate, we will estimate the defect production rate and the annihilation rate separately. The effects of deformation on the defect production in crystal solids have been discussed

Table 2. The values of the stress scaling exponent m defined by $\dot{\gamma} \sim \sigma^m$ for different systems.

System	m	Reference
CTAB/hexanol/water	2	Bohlin <i>et al.</i> [13]
SDS/pentanol/dodecane	1	Roux <i>et al.</i> [14]
8CB (31 °C)	2	Panizza <i>et al.</i> [15]
CpCl/hexanol/brine	1.67	Meyer <i>et al.</i> [8–10]
8CB (22–29 °C)	1.67	Meyer <i>et al.</i> [9,10]
P123/butanol/brine	1.67	Meyer <i>et al.</i> [10]
C ₁₀ E ₃ /D ₂ O	2	Oliviero <i>et al.</i> [16]
C ₁₂ E ₅ /water	1.44	present study

by Bruinsma *et al.* who predicted the shear-induced defect proliferation [19]. In that picture, the deformation enhances the dissociating rate of the bound pairs of defect lines, which then dissociate and move to reduce the applied strain.

In lamellar structures, many equilibrium defects are bound loops consisting of both screw and edge dislocations, so that the above mechanism should still operate. However, lamellar phases have a well-known dilation (or undulation) instability. This instability can generate far more defects than to dissociate the existing bound loops. The question is, why does instability happen during the flow? If the initial layers are already tilted so that the layer normal has a non-vanishing positive component along the flow direction, then the shear flow will tilt the layer normal toward the flow direction. The shear will also dilate the layer repeat distance. Therefore with the existing tilt, the layers are dilated and the tilting angle is increased by the shear continuously, so that when the tilt reaches a certain angle, the instability sets off and the layers are buckled.

This reasoning, however, fails when the sample starts with the homeotropic alignment, where the shear cannot tilt the layers as the layers are parallel to the local flow velocity. In the next subsection, we suggest that, when the applied shear stress drives the screw defects motion due to the Peach-Koehler force, these defect motions will tilt the layers, even when the layers are well aligned at the beginning. Once the layers are not at the perfect alignment, the shear flow can tilt and dilate it as mentioned above. The shear can now trigger the dilation instability to produce new defect lines. Thus the dislocation production in the lamellar liquid crystals is fundamentally different from that of the crystals. In the last part of this section, we estimate the (shear rate dependent) density and size of defect loops in the steady-shear condition. The defect line density is then related to the stress through the dissipation argument. The obtained shear thinning exponent $m = 3/2$ is found to be consistent with our experimental result as described in the previous section.

Among the possible configurations of line defects and walls, we will only consider the effect of the dislocation defect lines for simplicity. In fact, small-angle grain boundaries can also be viewed as an array of strongly bound line defects.

3.2 Defect motion and the layer tilting

Consider a lamellar sample aligned in the homeotropic orientation which is not tilted initially. The lamellar contains some defect lines. A shear is applied such that the layer normal unit vector \mathbf{n} is in the gradient direction $\hat{\mathbf{z}}$ to begin with. The defect lines are assumed to form dislocation loops, each consisting of two segments of screw dislocations (of length l_s) in the layer normal direction $\hat{\mathbf{z}}$ and two edge dislocations (of length l_e) within the velocity-vorticity plane.

Under the applied stress $\boldsymbol{\sigma}$, the defect lines are subjected to the Peach-Koehler force per unit length [2, 20, 21]

$$\mathbf{F}_{\text{PK}} = \boldsymbol{\tau} \times (\boldsymbol{\sigma} \cdot \mathbf{n} b), \quad (2)$$

where $\mathbf{n} b$ is Burgers' vector, and $\boldsymbol{\tau}$ the unit tangent vector of the defect line. To define Burgers' vector, one encloses the defect line by a closed loop where the net layer distortion after completing the loop defines Burgers' vector [2]. The equation transforms properly if one changes the signs of $\mathbf{n} b$ and $\boldsymbol{\tau}$ simultaneously. The stress $\boldsymbol{\sigma}$ does not include the self-stress from the defect itself [2]. The tension force \mathbf{f}_t from two ends of a defect line segment gives a net force per unit length $\mathbf{F}_t = \partial \mathbf{f}_t / \partial s$, where s is the arc-length of the defect line. The viscous force is $\mathbf{F}_v = \boldsymbol{\mu}^{-1}(\boldsymbol{\tau}) \cdot (\mathbf{v}(\mathbf{R}(s, t)) - \dot{\mathbf{R}})$, where $\boldsymbol{\mu}(\boldsymbol{\tau})$ is the orientation-dependent mobility matrix, $\mathbf{R}(s, t)$ the position of the defect line, and $\mathbf{v}(\mathbf{R}(s, t))$ the convection velocity at $\mathbf{R}(s, t)$. The arc-length variable s increases along the local tangent vector $\boldsymbol{\tau}$, so that $\boldsymbol{\tau} = \partial \mathbf{R}(s, t) / \partial s$. The force balanced condition

$$\mathbf{F}_{\text{PK}} + \mathbf{F}_t + \mathbf{F}_v = 0 \quad (3)$$

gives the defect line dynamic equation such that

$$\dot{\mathbf{R}} = \mathbf{v}(\mathbf{R}(s, t)) + \boldsymbol{\mu}(\boldsymbol{\tau}) \cdot (\boldsymbol{\tau} \times (\boldsymbol{\sigma} \cdot \mathbf{n} b) + \partial \mathbf{f}_t / \partial s). \quad (4)$$

Note that for a given loop geometry $\mathbf{R}(s, t)$, there are two possible defect orientations (depending on the sign of b), which move differently under the shear.

The mobility matrix $\boldsymbol{\mu}(\boldsymbol{\tau})$ depends strongly on the orientation and Burgers' vector. For screws where $\boldsymbol{\tau} = \pm \mathbf{n}$, the mobility is isotropic so that

$$\boldsymbol{\mu}(\mathbf{n}) = \mu_s (\mathbf{I} - \boldsymbol{\tau} \boldsymbol{\tau}), \quad (5)$$

where \mathbf{I} is the identity matrix, and μ_s the screw mobility. The screws could move easily so that μ_s is large [21]. The term $-\boldsymbol{\tau} \boldsymbol{\tau}$ is to emphasize that the line will not move along its tangent direction.

For the edge dislocation where $\boldsymbol{\tau} \perp \mathbf{n}$, the mobility is

$$\boldsymbol{\mu}(\boldsymbol{\tau}) = \mu_g \mathbf{n} \mathbf{n} + \mu_e (\mathbf{I} - \mathbf{n} \mathbf{n} - \boldsymbol{\tau} \boldsymbol{\tau}), \quad (6)$$

where μ_g and μ_e are the edge glide and climb mobilities, respectively. The latter can be measured, by using a wedge to induce the layer dilation. The climb motion is slower, being limited by the very dissipative permeation process. The edge glide mobility μ_g is even smaller than μ_e because

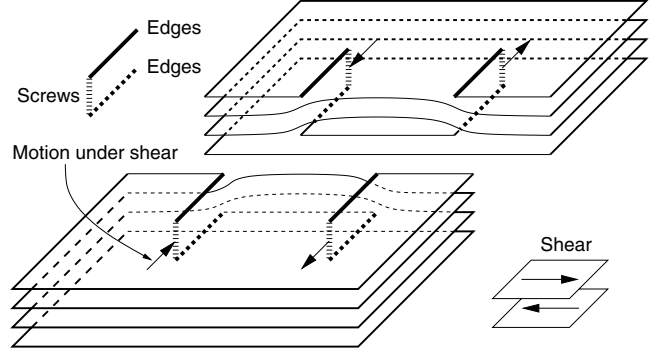


Fig. 7. The screw defects move under the applied shear, to increase or decrease the area of the defect loops.

gliding requires an activation process to initiate the layer reconnection. Below we will neglect the edge gliding and set $\mu_g \simeq 0$.

According to equation (4), the shear stress and its associated Peach-Koehler force induce the motion of the screws toward the vorticity direction. (The tilting effects on screws due to the shear convecting flow are most likely to be canceled by the screw line tension resisting tilting.) The two screws of a given closed loop will have opposite tangent $\boldsymbol{\tau}$, and hence the most important consequence is that they move in the opposite directions under the Peach-Koehler force. The area enclosed by the loop will either decrease or increase depending on the loop orientation, as shown in Figure 7.

We define the vector area per unit volume $\mathbf{p}(\mathbf{r}, t)$ as (similar to Eq. (9.50) of Ref. [2] but with the extra 1/2 factor)

$$\mathbf{p}(\mathbf{r}, t) = \frac{1}{2} \sum_i b_i \int \mathbf{R}_i(s_i, t) \times d\mathbf{R}_i(s_i, t) \delta^3(\mathbf{r} - \mathbf{R}_i(s_i, t)), \quad (7)$$

where i denotes the label for the defect loops. For example, the average $\mathbf{p}(\mathbf{r}, t)$ for N square loops, each with a normal pointing in the flow direction $\hat{\mathbf{x}}$ and a size of $l_s \times l_e$ inside a volume V , is $(l_s l_e N / V) \hat{\mathbf{x}}$. The loop area is also related to other ideas which consider the defect lines as a generalized “currents” [2] or “line charges” [22]. If one writes $d\mathbf{R}_i(s_i, t)$ in the above integral as $\boldsymbol{\tau}_i ds_i$, then $\mathbf{p}(\mathbf{r}, t)$ can also be interpreted as the moment of the line charge density $b_i \boldsymbol{\tau}_i \delta^3(\mathbf{r} - \mathbf{R}_i(s_i, t))$. If the defect loop is on the velocity gradient-vorticity plane, \mathbf{p} will point in the flow direction. In a well-aligned equilibrium sample, the defect loops of the two opposite orientations could have the same total area but opposite contributions to \mathbf{p} , so that the averaged \mathbf{p} vanishes in equilibrium.

Following from equation (7), the moment $\mathbf{p}(\mathbf{r})$ evolves as

$$\dot{\mathbf{p}}(\mathbf{r}, t) = \frac{1}{2} \sum_i b \int \left[\dot{\mathbf{R}} \times d\mathbf{R} + \mathbf{R} \times d\dot{\mathbf{R}} \right] \delta^3(\mathbf{r} - \mathbf{R}) - \mathbf{R} \times d\mathbf{R} (\dot{\mathbf{R}} \cdot \nabla) \delta^3(\mathbf{r} - \mathbf{R}), \quad (8)$$

where the subscript i is suppressed for clarity. The last term $\nabla \delta^3(\mathbf{r} - \mathbf{R})$ will be dropped as it is averaged to zero.

The second term can be rewritten, after integration by parts, as

$$\begin{aligned} \int \mathbf{R} \times d\dot{\mathbf{R}} \delta^3(\mathbf{r} - \mathbf{R}) &= - \int \frac{\partial \dot{\mathbf{R}}}{\partial s} \times \mathbf{R} \delta^3(\mathbf{r} - \mathbf{R}) ds \\ &= \int \dot{\mathbf{R}} \times \frac{\partial}{\partial s} (\mathbf{R} \delta^3(\mathbf{r} - \mathbf{R})) ds \\ &= \int \dot{\mathbf{R}} \times d\mathbf{R} \delta^3(\mathbf{r} - \mathbf{R}) \\ &\quad - \int \dot{\mathbf{R}} \times \mathbf{R} \boldsymbol{\tau} \cdot \nabla \delta^3(\mathbf{r} - \mathbf{R}) ds, \end{aligned} \quad (9)$$

where the first contribution is the same as the first term in equation (8). The second contribution is averaged to zero and will be neglected below. Together we get

$$\dot{\mathbf{p}}(\mathbf{r}, t) \simeq \sum_i b \int \dot{\mathbf{R}} \times d\mathbf{R} \delta^3(\mathbf{r} - \mathbf{R}). \quad (10)$$

Since the pure screw defect lines have much smaller energy than the tilted screw, the tensions force will keep the screws parallel to the layer normal \mathbf{n} . In such case, the two edges of a given loop must have the same velocity $\dot{\mathbf{R}}$, but they have opposite $d\mathbf{R}$. Therefore, for the edges, the term

$$\sum_{\text{edges}} b \int \dot{\mathbf{R}} \times d\mathbf{R} \delta^3(\mathbf{r} - \mathbf{R}) \quad (11)$$

is averaged to zero.

For the screws, their $d\mathbf{R}$ is parallel to \mathbf{n} . Since, for a given loop, there are two screws with opposite $d\mathbf{R}$, the contribution $\mathbf{v}(\mathbf{R}(s, t))$ in equation (4) for $\dot{\mathbf{R}}$ is the same for the two segments with opposite directions, so that their contributions average to zero. The tension term in equation (4) will shrink the loop areas for both types of loop orientations. If the screw densities are the same for both types of orientations, the net effect on $\dot{\mathbf{p}}$ also vanishes on average. Therefore the remaining Peach-Koehler force term will give the main contribution

$$\dot{\mathbf{p}}(\mathbf{r}, t) = \mathbf{K} \cdot (\boldsymbol{\sigma} \cdot \mathbf{n}). \quad (12)$$

Here the tensor \mathbf{K} is isotropic $\mathbf{K} \equiv (\mathbf{I} - \mathbf{nn})K$, with

$$K = \sum_{\text{screws}} \int b^2 \mu_s \delta^3(\mathbf{r} - \mathbf{R}(s, t)) ds = \langle b^2 \mu_s \rangle \rho_s, \quad (13)$$

where

$$\rho_s = \sum_{\text{screws}} \int \delta^3(\mathbf{r} - \mathbf{R}(s)) ds \quad (14)$$

is the screw density, and the angular bracket denotes the average over the defect lines. Physically, ρ_s is the surface number density of the crossings made by screw dislocations on a surface with its normal in the \mathbf{n} direction. If one regards the defect as a vector charge, \mathbf{K} consists of the multiplication of the charge density, mobility, and charge squared. The formula is similar to the one of the conductivity of the electrolyte solution so that \mathbf{K} can be viewed as a generalized conductance tensor.

To describe the layer orientation and the layer compression, one defines

$$\mathbf{m} = (d_0/d)\mathbf{n} \quad (15)$$

as the scaled wave vector variable, where d is the local distance between the two neighboring layers, and d_0 the equilibrium layer separation. Recall that \mathbf{m} represents the local layer compression, so that the integration along an arbitrary loop defines Burgers' vectors of the defect lines enclosed by the loop. In a differential form, it reads

$$\nabla \times \mathbf{m}(\mathbf{r}, t) = \sum_i \int b_i \boldsymbol{\tau}_i \delta^3(\mathbf{r} - \mathbf{R}_i(s_i, t)) ds_i, \quad (16)$$

as in equation (9.18) of reference [2].

Now it can be demonstrated how the change of defect loops area would cause the change of the average layer orientation by establishing the relationship between \mathbf{p} and \mathbf{m} . Using the identity $\epsilon_{abc} r_b \epsilon_{cde} \nabla_d m_e = 2m_a + \nabla_a (r_b m_b) - \nabla_b (r_b m_a)$, we write

$$\begin{aligned} \int_V m_a(\mathbf{r}, t) d\mathbf{r} &= \frac{1}{2} \int_V \epsilon_{abc} r_b \epsilon_{cde} \nabla_d m_e d\mathbf{r} \\ &\quad + \frac{1}{2} \int_{\partial V} (m_a r_b - m_c r_c \delta_{ab}) dA_b \\ &= \int_V p_a(\mathbf{r}, t) d\mathbf{r} \\ &\quad + \frac{1}{2} \int_{\partial V} (m_a r_b - m_c r_c \delta_{ab}) dA_b, \end{aligned} \quad (17)$$

where the term $\epsilon_{abc} r_b \epsilon_{cde} \nabla_d m_e$ (or $\mathbf{r} \times \nabla \times \mathbf{m}$) is transformed into $\mathbf{p}(\mathbf{r}, t)$ as

$$\begin{aligned} \frac{1}{2} \mathbf{r} \times \nabla \times \mathbf{m} &= \frac{1}{2} \mathbf{r} \times \sum_i \int b \boldsymbol{\tau} \delta^3(\mathbf{r} - \mathbf{R}(s, t)) ds \\ &= \frac{1}{2} \sum_i \int \mathbf{R}(s, t) \times b \boldsymbol{\tau} \delta^3(\mathbf{r} - \mathbf{R}(s, t)) ds \\ &= \mathbf{p}(\mathbf{r}, t). \end{aligned} \quad (18)$$

Equation (17) shows that the perturbation of the vector field $\delta\mathbf{p}$ will induce $\delta\mathbf{m}$. The Peach-Koehler force under the shear will induce $\delta\mathbf{p}$ along the velocity direction, which is perpendicular to the initial \mathbf{m} . Therefore the perturbation of the defect loop area (due to the screw motion under the shear), can cause the layer orientation (the \mathbf{m} direction) to tilt toward the flow direction. We finally obtain the evolution of \mathbf{m} as

$$\dot{\mathbf{m}}_{\text{PK}} = \mathbf{K} \cdot (\boldsymbol{\sigma} \cdot \mathbf{n}). \quad (19)$$

The important consequence is that, even starting from a strictly homeotropic aligned sample, equation (19) gives a $\dot{\mathbf{m}}_{\text{PK}}$ in the flow direction, leading to the layer tilting driven by the defect motions. A graphic illustration is shown in Figure 8. Furthermore the direction of tilting is the unstable one with which the shear flow will further increase the tilting toward the undulation instability. This

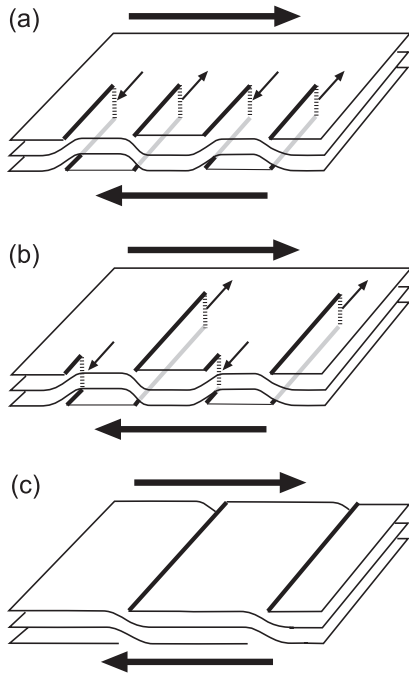


Fig. 8. Time sequence drawings to illustrate the layer tilting caused by the defect loop motion. The large arrows indicate the shear flow. The small arrows indicate the screw defect velocity. (a) The defects move under the applied shear. (b) As the screws move, the loop areas increase or decrease according to the loop orientations. (c) As a consequence of the screw defect motion, the layers are tilted.

sequence is illustrated in Figure 9a–c. Researchers have observed layer dilation under flow constantly. However, it is not obvious that a well-aligned layered structure with homeotropic orientation should encounter layer dilation. (Of course the slopped boundary plates may also cause dilation as the gap changes under shear.) Here we show that, as long as the layered structure has defect loops, it bounds to be tilted and dilated under the applied stress.

The dilation eventually leads to undulation instability and defect formations, with which the homeotropic and preferred layer spacing could be maintained. This undulation instability at the non-linear regime was indeed observed to produce edge dislocations parallel to the undulations [23,24]. Usually the defect formation involves the breaking of the layers, hence the outcomes are relatively noisy. The lamellar or smectic phases, however, show surprisingly regular pattern upon dilation instability. This suggests that the defect formation scheme might not have many variations. The mechanism could be close to the picture illustrated in Figure 9c–f. As shown in the sketch, the dilation caused by the shear flow eventually leads to instabilities and a pair of edge dislocations are produced such that the layers could align horizontal and restore their preferred layer spacings. In a real three-dimensional sample, the two edges are connected by two screws to form a dislocation loop. The orientation of these newly formed defect loops must be predominantly the one disfavored by the shear, so that \mathbf{m} , and hence the layer normal \mathbf{n} , can

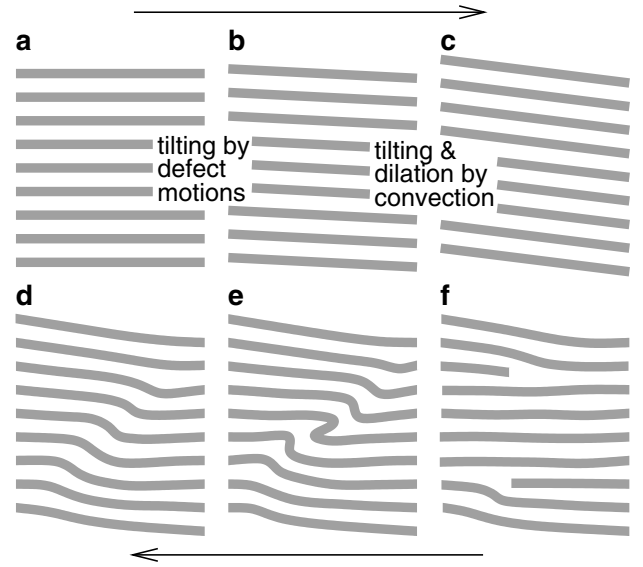


Fig. 9. Sequences of layer tilting by defect motions, convection-induced dilations, and defect formations. a→b: layers tilted by the changes of defect loop area due to screw motion (defect lines not shown for clarity). b→c: layers further tilted and dilated by convection. c→e: onset and development of the undulation instability. e→f: creation of new defect loop, with the edge segments running perpendicular to the paper and the screw segments (not shown) running vertically.

be restored to the homeotropic alignment, as illustrated in Figure 9f. This realignment to homeotropic thus gives an estimate of the minimal production rate of the screw defects by the instability mechanism.

Since the layers are first tilted by the defect motions and subsequently dilated by the shear flow, we thus postulate that, as $|\mathbf{m}|$ is decreasing with layer tilting, undulation instability happens at a particular tilting angle θ_c [25]. The production of the defect loops takes place at a frequency proportional to $\dot{\gamma}$. Experimentally, the fluctuating characteristics of such a sample might be similar to the oscillation in jamming of a colloid [26]. In the colloid system, it is indeed observed that the stress fluctuates with a characteristic time proportional to the inverse shear rate.

3.3 Screw density and the shear stress

Next we calculate the viscosity contributed by the defect loops. When the layers are sheared with a rate $\dot{\gamma}$, the defect loops could cause energy dissipation, mainly from the viscous force acting on edges by the shear flow. Let us assume a typical dislocation loop with screw lengths l_s and edge lengths l_e as defined before. We follow the argument by Oswald and Allain to estimate the dissipation from the viscous force [18]. The argument is also consistent with the equation (4) above. Each defect loop floats in the shear flow as a whole, so that $\dot{\mathbf{R}}$ becomes the same everywhere on the loop. However, the two edges are advected by the flow with the different velocities $\mathbf{v}(\mathbf{R}(s, t))$. Therefore the edges have to climb (driven by $\boldsymbol{\mu} \cdot \partial \mathbf{f}_t / \partial s$). The climb

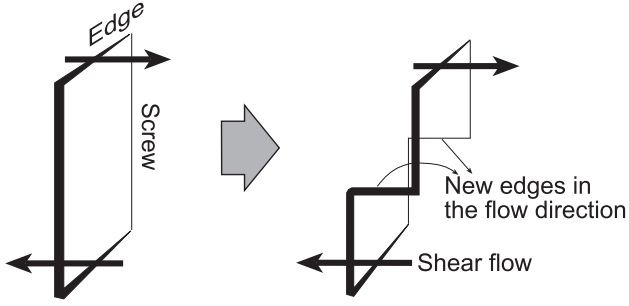


Fig. 10. Elongation of defect loops when the viscous force exceeds the edge line energy.

velocity has magnitude $|\dot{\mathbf{R}} - \mathbf{v}(\mathbf{R}(s, t))| = \Delta v = l_s \dot{\gamma} / 2$ for both edges. The viscous force on the edge is therefore $f_v = l_e |\mathbf{F}_v| = l_e \Delta v / \mu_e$. The dissipation per unit volume $T \dot{s}$ gives the scaling of the effective viscosity η_{eff} as

$$T \dot{s} \simeq \eta_{\text{eff}} \dot{\gamma}^2 \simeq n_0 \Delta v f_v \simeq \left(\frac{n_0 l_s^2 l_e}{\mu_e} \right) \dot{\gamma}^2, \quad (20)$$

where n_0 is the number density of the loops.

To balance the desired viscous force, where $\dot{\mathbf{R}}$ is the same for the loop, the required tension f_s is

$$f_s \simeq \frac{l_s l_e \dot{\gamma}}{\mu_e}. \quad (21)$$

The actual tension has magnitude $l_e |\mathbf{F}_t| \simeq \tau_e$ which is the energy per unit length of the edge dislocation. If $f_s > \tau_e$, the actual tension is not strong enough to maintain the constant $\dot{\mathbf{R}}$ for both edges, and two new edge segments along the flow direction will be produced, as illustrated in Figure 10. This leads to a continuous elongation in the flow direction. Such deformed loops may collide with other defect lines, causing defect annihilation and reducing loop sizes.

Right after the undulation instability, we thus expect the formation of defect loops with long edges. However they will encounter huge viscous forces on the screws if they were able to maintain the stationary shape. The actual tension is unable to match the magnitude. Therefore the large loops only appear in transient, *i.e.*, they must be reconnected or pair-annihilated. The pair annihilation requires matched Burgers' vectors and hence happens slowly. We assume that during the short transient period, the large loops collide and reconnect to form many small loops, so that after the reconnection, the defect loops are small enough to reach the balance $f_s \simeq \tau_e$. We assume that the cascade of defect reactions eventually constraints the defect loop areas so that

$$\frac{l_s l_e \dot{\gamma}}{\mu_e} \simeq \tau_e, \quad (22)$$

i.e., the line energy is able to maintain the loop geometry in the shear flow. A similar steady-state consideration of whether the loop will be tilted by the flow leads to a similar scaling, with τ_e replaced with the screw line tension.

Combining equations (20) and (22), the stress $\sigma = \eta_{\text{eff}} \dot{\gamma}$ becomes

$$\sigma \simeq \rho_s \left(\frac{l_s l_e \dot{\gamma}}{\mu_e} \right) \simeq \rho_s \tau_e, \quad (23)$$

where we have used the identity $\rho_s = l_s n_0$.

3.4 Shear thinning behavior

We then consider how the shear rate affects the defect density. Suppose that the instability happens at a particular tilting angle θ_c and that the instability creates certain new defect loops, of density Δn_0 . The loop area produced $\Delta n_0 l_s l_e$ must be at least θ_c / b , so that the layers are tilted back (to the homeotropic alignment). In other words, this is a lower bound estimation and any lower defect production rate will not be able to maintain the area balance between the two types of loop orientations. The characteristic time between two instabilities is $\Delta t = \theta_c / \dot{\gamma}$. Recall that $\Delta \rho_s = l_s \Delta n_0$, which leads to the production rate of ρ_s as

$$\frac{\Delta \rho_s}{\Delta t} = \frac{\dot{\gamma}}{b l_e}. \quad (24)$$

These rectangular loops are convected by the shear flow. For a particular loop, there is a distance ξ in the flow direction to the next loop whose central position is shifted vertically not larger than l_s (so that they have a chance of colliding). Since two colliding loops on average have a vertical position separation of l_s , their relative velocity under shear flow is $\dot{\gamma} l_s$. The colliding rate is thus $\dot{\gamma} l_s / \xi$ and the complete rate equation for ρ_s is

$$\frac{\partial \rho_s}{\partial t} = \frac{\dot{\gamma}}{b l_e} - \frac{\dot{\gamma} l_s}{\xi} \rho_s. \quad (25)$$

With $\rho_s \simeq \xi^{-2}$, we obtain in the steady state as

$$\rho_s \simeq \left(\frac{1}{b l_s l_e} \right)^{2/3} \simeq \left(\frac{\dot{\gamma}}{b \mu_e \tau_e} \right)^{2/3}, \quad (26)$$

where we have used equation (22). The scaling exponent of $2/3$ on the shear rate $\dot{\gamma}$ originates from the fact that the loop number density increases with $\dot{\gamma}$ but, on the other hand, the loop size decreases with $\dot{\gamma}$ because of the limited line tension support. From equation (23), we obtain the scaling relation

$$\dot{\gamma} \simeq \frac{b \mu_e}{\tau_e^{1/2}} \sigma^{3/2}. \quad (27)$$

Hence we get the exponent $m = 3/2$ as mentioned in Section 2 and the rheology response is a shear thinning behavior.

The line energy of the edge defect contains the elastic energy contribution, which is sensitive to the defect core structure. The integrated energy depends on the short-distance cut-off as detailed in reference [2]. When Burgers' vector is smaller than the penetration length $\sqrt{K_s / B}$, where K_s is the saddle-splay elastic constant and B the layer compression modulus, we use the penetration length

as the cut-off to estimate $\tau_e \sim Bb^2$. Then the above relation is further simplified as

$$\dot{\gamma} \simeq \frac{\mu_e}{B^{1/2}} \sigma^{3/2}, \quad (28)$$

which depends only on μ_e and B , and is independent of b . When the averaged Burgers' vector is larger than the penetration length $\sqrt{K_s/B}$, the cut-off is set to Burgers' vector, and the edge energy becomes $\tau_e \sim b\sqrt{K_s B}$. We then obtain instead

$$\dot{\gamma} \simeq \frac{b^{1/2}}{(K_s/B)^{1/4}} \frac{\mu_e}{B^{1/2}} \sigma^{3/2}. \quad (29)$$

The obtained shear thinning exponent $m = 3/2$ is compared with our experimental result in Figure 6 together with the prediction by Meyer *et al.* $m = 5/3$ [9,10]. Other experimental values of m are listed in Table 2. They scatter between 1 and 2. Interestingly, the material 8CB measured at a slightly different temperature shows clearly different exponents [10,15]. The exponent $m = 2$ is reported for the higher temperature where the system is just a few degree lower than the smectic-nematic transition point [15]. The smaller exponent $m = 1.67$ is reported for a lower temperature sample [10]. It will be certainly helpful to have more systematic study on the lamellar and smectic rheology behavior.

If we put some typical numbers into equation (28) such as $\mu_e \simeq 10^2 \text{ m s kg}^{-1}$, $B \simeq 10^6 \text{ Pa}$ [27], $\sigma \simeq 0.5 \text{ Pa}$, we obtain $\dot{\gamma} \simeq 0.035 \text{ s}^{-1}$. This value is slightly smaller than the measured shear rate $\dot{\gamma} \approx 0.5 \text{ s}^{-1}$ but gives roughly a reasonable order. Another estimate of $B \simeq k_B T/d_0^3 \simeq 10^4 \text{ Pa}$ would yield $\dot{\gamma} \simeq 0.35 \text{ s}^{-1}$. One possibility for the low value is that the sample has larger Burgers' vectors, so that one should use equation (29) instead. Using the value $b \simeq 2 \text{ nm}$ [18], and the above shear rate, we get the average distance between screw dislocation ξ to be roughly 2–3 μm . The order of magnitude for ξ matches the distance seen in the previous experiment [10].

4 Texture visualization

We also performed some texture visualization of our samples. For the optical crossed-polars microscopy observation under shear flow, we used CSS-450 from Linkam Scientific Instruments, Ltd. The gap between the two plates was 200 μm . The pictures were taken at constant shear rates.

In Figures 11 and 12, we show the observed micrographs under shear flow. The shear rate is $\dot{\gamma} = 0.5 \text{ s}^{-1}$ for $\phi = 35 \text{ wt}\%$, and $\dot{\gamma} = 1 \text{ s}^{-1}$ for $\phi = 45 \text{ wt}\%$. For $\phi = 45 \text{ wt}\%$ sample, the elongated objects oriented along the flow in the steady state are typical oily streaks. The structure observed here is similar to that of Meyer *et al.* for 8CB [10].

For $\phi = 35 \text{ wt}\%$ sample, the elongated objects oriented with a small angle with respect to the flow in the steady state. The structure is somewhat different from the typical oily streaks. The elongated objects seem to be densely

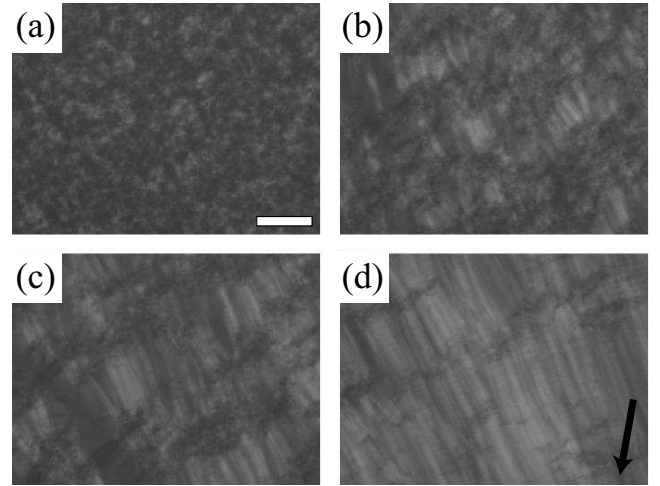


Fig. 11. Optical crossed polars micrographs under shear flow. The concentration of C_{12}E_5 is $\phi = 35 \text{ wt}\%$ and the shear rate is $\dot{\gamma} = 0.5 \text{ s}^{-1}$. (a) 0 min, (b) 3 min, (c) 5 min, (d) 10 min. The scale bar in (a) is 100 μm and the flow direction is indicated by an arrow in (d). The flow gradient direction is perpendicular to the paper.

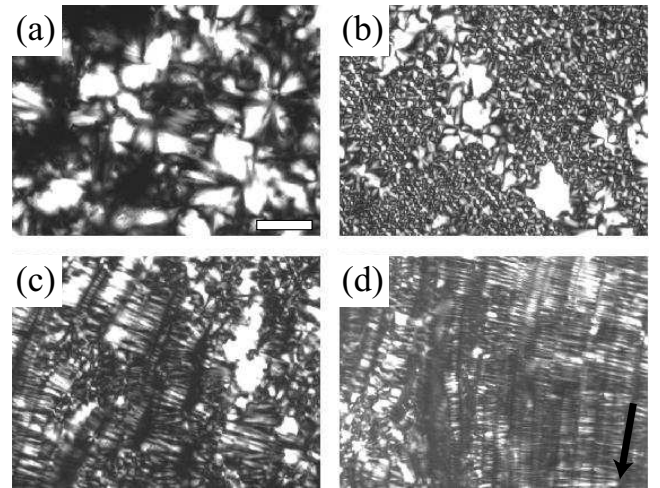


Fig. 12. Optical crossed polars micrographs under shear flow. The concentration of C_{12}E_5 is $\phi = 45 \text{ wt}\%$ and the shear rate is $\dot{\gamma} = 1 \text{ s}^{-1}$. (a) 0 min, (b) 5 min, (c) 10 min, (d) 15 min. The scale bar in (a) is 100 μm and the flow direction is indicated by an arrow in (d).

packed thin bright lines of few hundred microns in length. There are dark regions at which the bright lines terminate. The dark regions tend to align along the direction perpendicular to the thin lines. We are unable to fully explain the observed texture. More study in the future will help the detailed modeling. It is possible that these bright lines are densely packed, weakly contrasted oily streaks, and the dark regions contain screw defects. This is because the oily streaks come from the partial merging between two edge defects with Burgers' vectors of opposite signs. (The fully merged two edges will become a simple edge.) The $\phi = 35$ and 45 wt% might have oily streaks with different extent of merging, which affects optical appearance.

For $\phi = 30$ and 40 wt% samples, the structures are similar to that of $\phi = 35$ wt% sample. In the $\phi = 40$ wt% sample, we also see that some typical oily streaks appear together with the thin lines (presumably edge defects) in a parallel way. As the system reaches steady state, the number of typical oily streaks decreases.

The defect textures correlate strongly with the rheological shear thinning exponent. At smaller ϕ the observed exponents are close to the theoretical prediction, albeit the observed textures are more complex than the simple edge defects modeled in the theory. The theory proposed above does not work well for $\phi = 45$ wt%, and there the textures are different from the ones of other concentrations.

5 Discussion

Several points merit further discussion. The theory proposed assumes that the interaction between the screw defects is much smaller than the Peach-Koehler force. This includes the line-tension-induced attraction between the two screws connected by the edges, and the direct interaction between the defect lines. In the optical microscope visualization, we observe the fine texture with dark lines, probably indicating the cluster of the defect lines. It is not clear how the defect interaction affects the rheology behavior. Nonetheless, the measured shear exponent is not too far from the proposed simple picture which does not take into account defect interaction. This may indicate that the defect density scaling is close to the one estimated here. However, our estimations for the defect production and the annihilation rates are both too high. Within the allowed time window, no defect texture coarsening happens once they reach the steady-state density. We are unable to identify any sign of a dynamic balance between the defect production and the defect annihilation.

Next we discuss the similarities and the differences between the present theory and the one by Meyer *et al.* [9,10]. Similar assumptions for both theories are: i) The two theories both assume that the screw defects move according to the Peach-Koehler force. ii) Both theories consider that the plastic deformation is due to defect motion. The plastic layer tilting rate here (see Eq. (19)) is similar to the combination of the Peach-Koehler force and the Orowan relation there.

However there are important differences which lead to different mechanisms for rheology responses: i) In the present theory we predict that the plastic deformation will lead to instability, as the layer tilting driven by the Peach-Koehler force is toward the unstable direction. In the theory of references [9,10], they concluded that the sign of the plastic deformation helps to stabilize the layer. Therefore even under the shear flow deformation which leads to instability for a tilted layer, their theory assumes that the instability does not happen. ii) In our theory, the plastic deformation is only important initially, which sets up the initial layer tilting. After the initial tilting, we assume that the shear deformation dominates. In the theory of references [9,10], the plastic deformation rate is the same as the flow deformation rate all the time. iii) The

defect line density is determined differently. In their theory the applied stress is mainly balanced by the internal stress, which comes from the interaction between the screw defect lines. This condition fixes the screw density in references [9,10]. In the present theory we ignore the interaction between the screws. The defect density here is determined by the balance between the production and annihilation processes as in equation (25). iv) The defect organizations are assumed differently. We assume that the defect interaction is screened so that the defect is free to move under the applied force; whereas in their theory the defect lines interaction is important, which provides the internal stress under applied stress. Nevertheless, the defect line can still move. In other words, we consider the defects as in the “liquid state”, whereas they seem to view defects as in the “glass state” which has the shear modulus due to defect interaction. v) Two theories have considered different dissipation mechanisms. The dissipation here is due to the permeation which happens when the mass flow passes through the edge defects. In their theory the external force has to do work against the internal stress to move the defects. If these two mechanisms are both important, the sum of their dissipation should be considered. vi) As pointed out in iii), the stress in references [9,10] has an elastic nature, whereas in our theory the stress is assumed to have viscous origin. Further stress relaxation experiments after the shear rate jump may give useful information to identify the nature of the stress.

In Section 2, we have measured a relatively large activation energy, $65k_B T_R$. The large activation energy in this system indicates a collective process involved in the flowing condition. The shear flow imposed on a standing defect loop causes an edge climb motion relative to its local environment. The climb of an edge requires the surfactant to diffuse to or away from the layers containing the defect edges. This diffusion, or permeation, has a flux normal to the layer. When the permeation flux involved an activation process, the permeation coefficient contains the activation energy. Three possibilities come to mind. i) The first possible path requires the surfactant to dissolve into the water, diffuse to the other layer, and readsorb into the bilayer. If that is the dominant path, then the activation energy corresponds to the energy barriers for a surfactant molecule to dissolve or readsorb into the bilayers. One expects that the activation energy comes from the van der Waals attraction or the hydrophobic/hydrophilic energy. The experimental value, however, seems much too large for this single molecule interpretation. ii) The second possible pathway is that the dissolving process involves more than one surfactant molecule, to act collectively. The dissolved molecules may form a small micelle directly. This collective process may be similar to the vesicle budding process in lipid bilayers. iii) The third possible pathway for the permeation flux is that the adjacent bilayer can form a neck to fuse and then break up, which facilitates the exchange of molecules between the layers. If the second or the third collective processes have a higher rate than the single molecule process, they may dominate the viscosity and become very sensitive to the temperature. The third process is similar to the relaxation of the surfactant

sponge phase, where the neck forming and breaking relaxation can be monitored by neutron scattering [28], and the activation energy can also be measured.

6 Conclusion

The shear thinning behavior is measured for the lamellar phase of the $C_{12}E_5$ /water system. The shear thinning exponent depends on the concentration. A simple rheology theory of lamellar phase is proposed with the relation $\dot{\gamma} \sim \sigma^m$, with $m = 3/2$. In the theory, we have shown that the defect-mediated layer tilting and dilation under shear flow could cause continuous production of dislocations. This picture explains the source of the defects. For concentration around 30 wt%, the shear thinning exponent is close to our theoretical estimation. Whereas at a higher concentration, close to 45 wt%, the exponent becomes smaller. The optical texture observation indicates that the texture changes very much with the concentration. This confirms that the defect texture could be responsible for the rheological behavior.

This work started when CYDL was visiting KITP at UCSB. He also acknowledges support by the National Science Council of Taiwan. SK and TK acknowledge support by KAKENHI (Grant-in-Aid for Scientific Research) on Priority Areas "Soft Matter Physics" and Grant No. 18540410 from the Ministry of Education, Culture, Sports, Science and Technology of Japan. We thank Prof. M. Imai for his help on the experimental part of the present work.

References

1. R.G. Larson, *The Structure and Rheology of Complex Fluids* (Oxford University Press, Oxford and New York, 1999).
2. P.G. de Gennes, J. Prost, *The Physics of Liquid Crystals* (Pergamon Press, Oxford, 1994).
3. F. Schneider, Phys. Rev. E **74**, 021709 (2006).
4. K. Kawasaki, A. Onuki, Phys. Rev. A **42**, R3664 (1990).
5. G.F. Mazenko, S. Ramaswamy, J. Toner, Phys. Rev. Lett. **49**, 51 (1982); Phys. Rev. A **28**, 1618 (1983).
6. S.T. Milner, P.C. Martin, Phys. Rev. Lett. **56**, 77 (1986).
7. G. Basappa, Suneel, V. Kumaran, P.R. Nott, S. Ramaswamy, V.M. Naik, D. Rout, Eur. Phys. J. B **12**, 269 (1999).
8. C. Meyer, S. Asnacios, C. Bourgaux, M. Kleman, Mol. Cryst. Liq. Cryst. **332**, 531 (1999).
9. C. Meyer, S. Asnacios, C. Bourgaux, M. Kleman, Rheol. Acta **39**, 223 (2000).
10. C. Meyer, S. Asnacios, M. Kleman, Eur. Phys. J. E **6**, 245 (2001).
11. B. Tamamushi, Rheol. Acta **13**, 247 (1974).
12. R.W. Duke, L.L. Chapoy, Rheol. Acta **15**, 548 (1976).
13. L. Bohlin, K. Fontell, J. Colloid Interface Sci. **67**, 272 (1978).
14. D. Roux, F. Nallet, O. Diat, Europhys. Lett. **24**, 53 (1993).
15. P. Panizza, P. Archambault, D. Roux, J. Phys. II **5**, 303 (1995).
16. C. Oliviero, L. Coppola, R. Gianferri, I. Nicotera, U. Olsson, Colloids Surf. A **228**, 85 (2003).
17. R. Strey, R. Schomäcker, D. Roux, F. Nallet, U. Olsson, J. Chem. Soc. Faraday Trans. **86**, 2253 (1990).
18. P. Oswald, M. Allain, J. Colloid Interface Sci. **126**, 45 (1988).
19. R. Bruinsma, B.I. Halperin, A. Zippelius, Phys. Rev. B **25**, 579 (1982).
20. L.D. Landau, E.M. Lifshitz, *Theory of Elasticity* (Pergamon Press, Oxford, 1987).
21. M. Kleman, O.D. Lavrentovich, *Soft Matter Physics: An Introduction* (Springer-Verlag, New York, 2003).
22. D.R. Nelson, J. Toner, Phys. Rev. B **24**, 363 (1981).
23. M. Delaye, R. Ribotta, G. Durand, Phys. Lett. **44**, 139 (1973).
24. L. Qiao, K.I. Winey, D.C. Morse, Macromolecules **34**, 7858 (2001).
25. Here we assume that θ_c may depend on the sample thickness, but not on the shear rate. According to this picture, both the averaged tilting angle $\langle \theta \rangle \simeq \langle n_x \rangle \simeq \theta_c$, and the frequency of the stress fluctuation ω_σ depend on the sample thickness. However we expect that $\omega_\sigma \sim \dot{\gamma} \langle n_x \rangle$ holds for different sample thicknesses.
26. D. Lootens, H. van Damme, P. Hébraud, Phys. Rev. Lett. **90**, 178301 (2003).
27. P. Oswald, M. Allain, J. Phys. (Paris) **46**, 831 (1985).
28. L. Porcar, W.A. Hamilton, P.D. Butler, G.G. Warr, Phys. Rev. Lett. **93**, 198301 (2004).